



Design, Analysis, and Verification of a 50-mm Push/Traction Sabot

by Brett Sorensen

ARL-TR-2292

August 2000

Approved for public release; distribution is unlimited.

DTIC QUALITY INSPECTED 4

20001030 133

The findings in this report are not to be construed as an official Department of the Army position unless so designated by other authorized documents.

Citation of manufacturer's or trade names does not constitute an official endorsement or approval of the use thereof.

Destroy this report when it is no longer needed. Do not return it to the originator.

Abstract

This report presents the design and analysis of a kinetic energy projectile for a 50-mm cannon using finite element techniques. A combination of push and traction launch concepts was used to configure a sabot for a penetrator that experienced catastrophic failure using a push launch sabot system. A parametric model with both plasticity and nonlinear elements was used to model the projectile that experienced accelerations exceeding 50,000 g's. Experimental tests showed marginal success in that a sabot failure permitted significant plastic deformation of the penetrator. Additional post-test analyses predicted the failure mode and the amount of plastic penetrator deformation demonstrated in the experiments.

Table of Contents

	<u>Page</u>
List of Figures	v
List of Tables	vii
1. Introduction	1
2. Design and Analysis	3
3. Experimental Verification	12
4. Post-Test Analyses	15
5. Conclusions	19
6. References	21
Distribution List	23
Report Documentation Page	27

INTENTIONALLY LEFT BLANK.

List of Figures

<u>Figure</u>	<u>Page</u>
1. Flash Radiographs of a Successful and Unsuccessful Push Launch Projectile	2
2. Profile of the Penetrator Used in Figure 1	2
3. Illustrations of Push and Traction Launch Sabot Systems	3
4. Simplified Projectile Geometry Profile Used to Construct the Parametric Model	4
5. CONTAC48 Element Definition	6
6. Nodal Plot With Boundary Conditions; Contact Surfaces Have Been Highlighted	7
7. Effective Stress and Plastic Strain Results of the Final Projectile Design	8
8. Plastic Strains and Penetrator Forces as a Function of Gap Size	11
9. Photograph of the Third Projectile Tested (Experiment No. 920)	13
10. Flash Radiograph of Experiment No. 920 at Muzzle Exit	13
11. Flash Radiograph of Experiment No. 918 Just Before Target Impact	14
12. Flash Radiograph of Experiment No. 919 Just Before Target Impact	14
13. Flash Radiograph of Experiment No. 920 Just Before Target Impact	14
14. Shear Stress and Effective Plastic Strain Results Using Exact Groove Geometry	16
15. Solid Model Used in a Groove Stiffness Analysis to Determine K_1 and F_{slide}	17
16. Displacement and Effective Plastic Strain Plots of the Penetrator Tail Deformation Analysis	18

INTENTIONALLY LEFT BLANK.

List of Tables

<u>Table</u>	<u>Page</u>
1. Results of the CONTAC48 Stiffness Study	6
2. Material Properties	7
3. Results From the Gap Size Study	10
4. Experimental Results	13

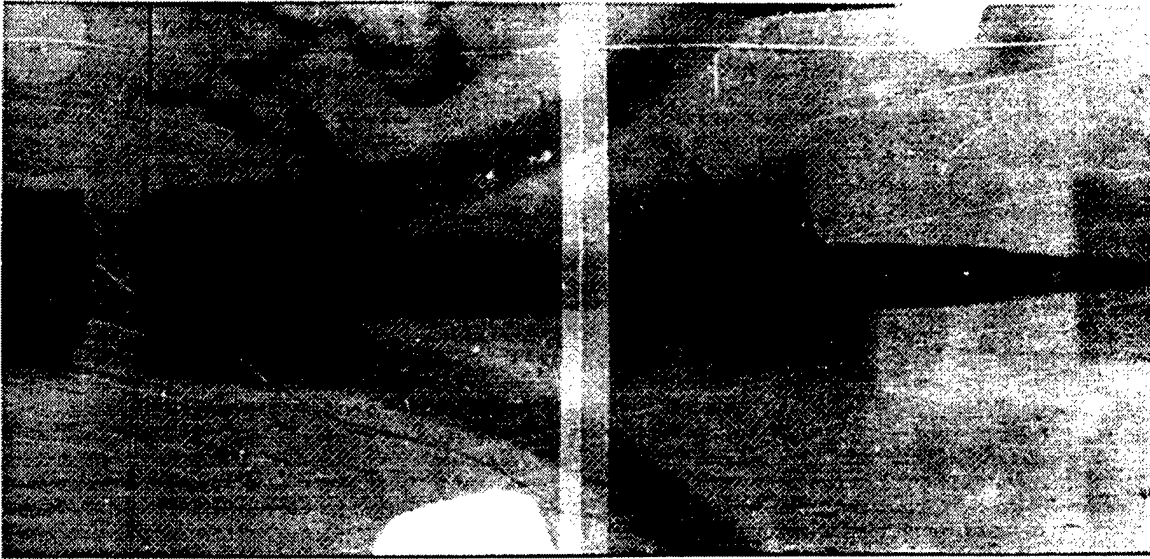
INTENTIONALLY LEFT BLANK.

1. Introduction

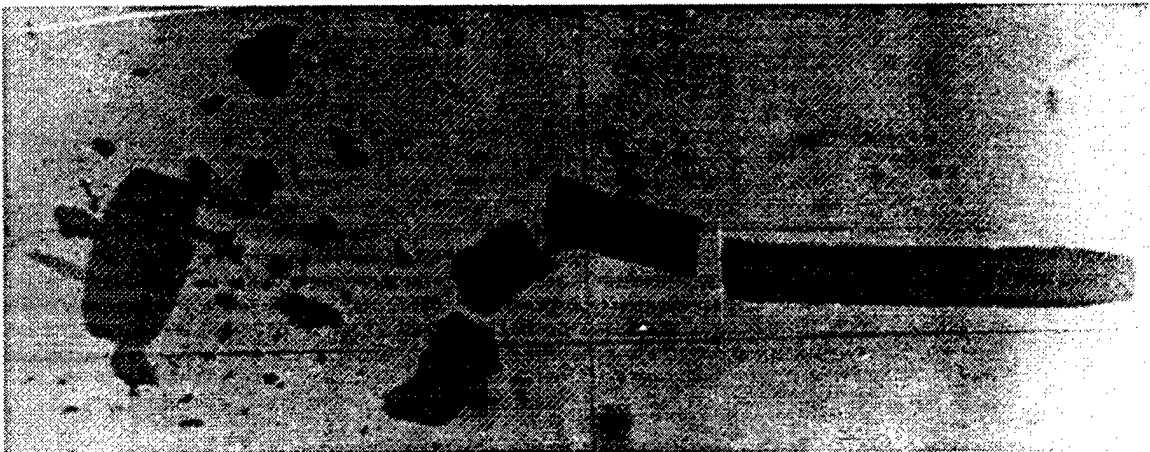
During a terminal ballistic testing program conducted at the U.S. Army Research Laboratory, a push-launched projectile package using a plastic (Nylon 6/6) sabot experienced catastrophic penetrator failure (see Figure 1). An elastic analysis showed that the maximum compressive stress in the tungsten alloy penetrator was at least 2.5 times the yield. Under slightly less severe conditions, a cylindrical penetrator would normally deform locally by barreling or with the formation of a mushroom at the interface with the pusher plate. However, a geometric feature at the aft end of the penetrator (see Figure 2) was assumed to create a stress riser. The stress riser, combined with the increased load, initiated a shear failure and caused substantial breakup of the remainder of the penetrator. Therefore, in order to complete the test sequence, either a penetrator modification or a different sabot was required to provide structurally secure launches.

Since the penetrator modification proved only partially successful, a different sabot concept was required—one that would minimize impact on the program. Figure 3 illustrates traditional push and traction launch systems. The traction sabot was considered too expensive and time intensive to manufacture; therefore, the push launch system required modification. Constrained by the penetrator design, manufacturing limitations, test requirements, and time, an aluminum sabot was conceived, which used annular grooves to engage with the forward portion of the penetrator. The hypothesis was that the sabot would be used to pull a portion of the penetrator while the pusher plate pushed the remainder, sufficiently modifying the inertial loads on the penetrator to reduce the stresses to acceptable levels.

To obtain a mass-efficient sabot that would properly support the penetrator, the ANSYS engineering analysis code [1] was used to generate a parametric model of the projectile and conduct finite element analyses. Nonlinear materials and contact elements were incorporated into the model to account for the plastic deformation and contact between the penetrator, sabot, and pusher plate. Multiple iterations on sabot geometry were conducted to obtain an acceptable solution with moderate risk. Included in the design process was a sensitivity study conducted on a critical dimension to



(a) Successful Test Conducted at a Lower Velocity and Acceleration



(b) Unsuccessful Test Conducted at Full Velocity and Acceleration

Figure 1. Flash Radiographs of a Successful and Unsuccessful Push Launch Projectile.

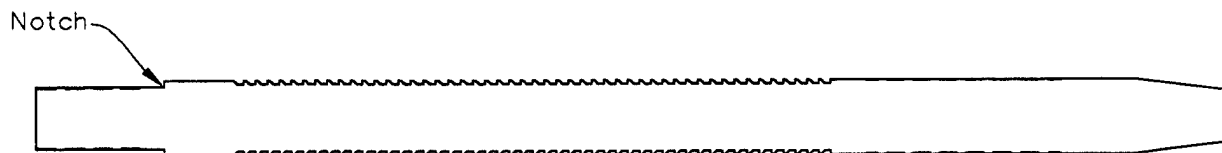


Figure 2. Profile of the Penetrator Used in Figure 1.

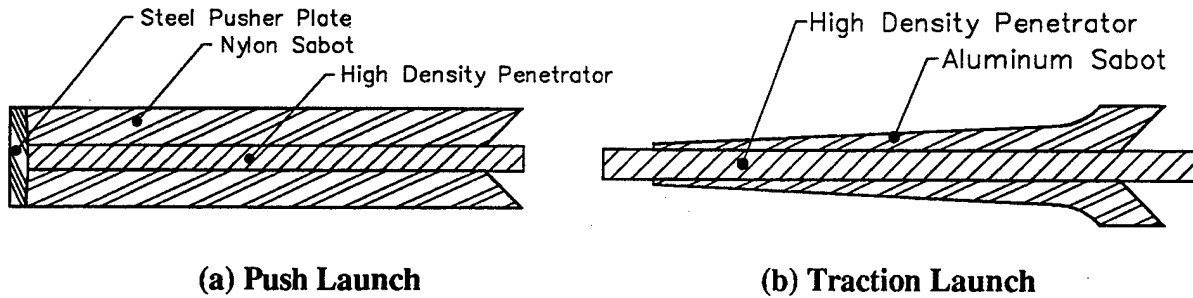


Figure 3. Illustrations of Push and Traction Launch Sabot Systems.

determine the necessary manufacturing tolerances and allowances. Regardless, the best solution observed was considered marginally secure.

Initial results (as seen from flash radiographs) indicated that the new sabot design appeared to function properly. However, after careful examination of the striking radiographs, it was determined that the penetrator was shorter than expected. Further analysis lead to the assumption that the sabot grooves had failed prior to maximum acceleration. With the sabot providing only radial restraint, the tail of the penetrator plastically deformed (but did not fail), which accounted for the decreased length. To verify these assumptions, finite element analyses of both the sabot groove failure and the penetrator tail deformation process (i.e., a projectile with the grooves removed) were performed. Results from these analyses indicate that the sabot grooves did fail; the penetrator deformation that resulted (including the decreased length) matched the radiograph, which confirmed the failure mechanism.

2. Design and Analysis

The first step in the design process was to conceptualize a design and make the necessary simplifications to construct a finite element model. Figure 4 displays the geometry profile for the initial solid model. The penetrator grooves have been removed and the nose details modified to create a simple cylindrical penetrator with a step decrease in diameter at the tail. Penetrator length was also modified to maintain the appropriate mass. The aluminum sabot is similar to the plastic

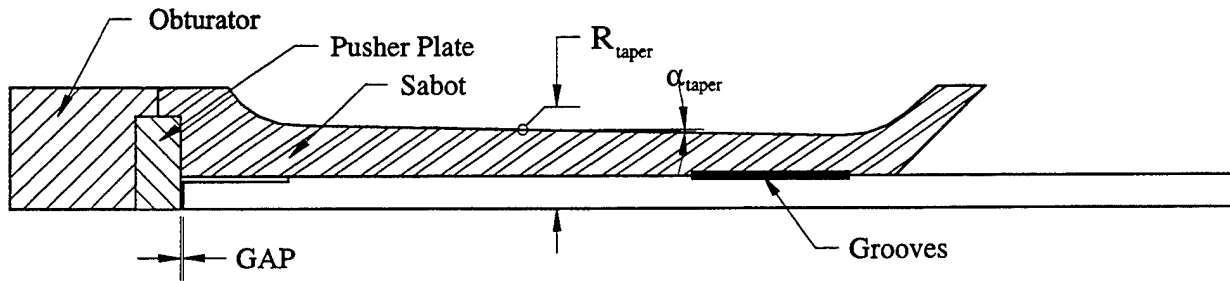


Figure 4. Simplified Projectile Geometry Profile Used to Construct the Parametric Model.

pusher-type sabot with two exceptions: (1) material has been removed to lighten the structure, creating a saddle between the two bore riding surfaces and (2) annular grooves attach to the forward portion of the penetrator. In this initial model, the grooves at the penetrator/sabot attachment are modeled by a shared-node interface. In addition to the groove interface, several other important interfaces between the penetrator, sabot, and pusher plate needed to be considered. These interfaces were modeled with contact surfaces to prevent undesired nodal penetrations between different materials, while permitting appropriate displacements. The remaining, less critical interfaces between the obturator, pusher plate, and sabot were modeled as shared-node boundaries to minimize the number of contact surfaces.

As mentioned before, the model was constructed in a parametric fashion. This was done to permit easy modification of the geometry to obtain a feasible solution with an acceptable mass. Although each feature required one or more variables for definition, three parameters were of greater importance during the study. First, a parameter specifying the gap between the penetrator and the pusher plate defined the amount of deformation that the sabot experienced prior to contact between the penetrator and pusher plate. Second, two parameters were used to define the saddle of the sabot, which determined both the mass of the sabot and the effective spring constant between the pusher plate and the forward portion of the penetrator supported by the sabot grooves. Using the sabot as a spring, the grooves would support the entire inertial load of the penetrator until the acceleration sufficiently compressed the sabot to cause the penetrator tail to contact the pusher plate. At this point, the penetrator would be supported by both the sabot and the pusher plate, redistributing the

strain in the penetrator. By varying these three parameters and examining the resulting stresses, a working design was achieved.

The model was meshed with four-node quadrilateral elements (SOLID42) and 2-D contact elements (CONTAC48). To examine mesh sensitivity, linear-elastic material properties were initially used. This permitted error prediction methods to economically size elements and therefore minimize errors due to mesh discretization. The mesh was adapted manually so that minor sabot geometry variations could be examined simultaneously; once an adequate mesh was obtained, a slightly optimized sabot would also have been obtained. The boundary conditions used during this process included an axial constraint on the front of the penetrator, radial constraints at the bore diameter, a pressure on the back of the obturator, and the appropriate axial acceleration to balance the forces at the axial constraint.

Once an acceptable mesh and sabot profile were obtained, the stiffness of the contact elements, the load profile, and the solution options were modified until convergence occurred in a timely manner with acceptable results. To verify that the appropriate stiffness was used on the contact elements between the penetrator and pusher plate, the stiffness was varied over five orders of magnitude, which allowed for studying the effects on node penetration, contact force, and strain. This was necessary because the CONTAC48 element uses the penalty function method to determine contact forces. A penalty stiffness is defined, acting normal to the target surface (see Figure 5), to enforce displacement compatibility by limiting the penetration of the contact node into the target surface. Higher stiffnesses lead to smaller penetrations, which increased the accuracy at the expense of additional solution time. Table 1 presents the results of this study and shows the maximum and average force in the contact elements, the amount of node penetration, the number of solution phase iterations required to resolve the loads, and the predicted error (due to mesh discretization) in both the penetrator and the sabot. The results show that as stiffness increases, node penetration decreases at the expense of additional iterations and increasing maximum contact forces. Since the average, and thus total contact force remains constant, the increasing maximum contact force introduced higher strains at certain discrete locations than what may have actually existed. The maximum contact forces on the mesh occurred at locations where nodes on either side of the contact surface

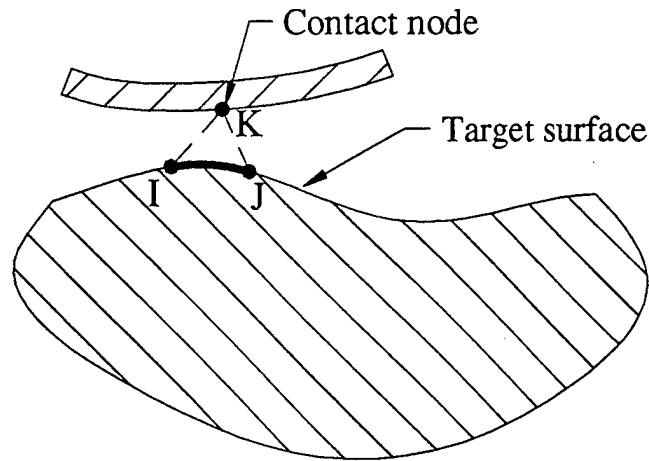


Figure 5. CONTAC48 Element Definition.

Table 1. Results of the CONTAC48 Stiffness Study

Stiffness (N/m)	Normal Force (Max.) (N)	Normal Force (Avg.) (N)	Node Penetration (Avg.) (m)	No. of Iterations	% Error in Mesh (Penetrator)	% Error in Mesh (Sabot)
1E7	.32E4	.27E4	-.28E-3	43	8.8	8.1
1E8	.51E4	.27E4	-.27E-4	51	8.4	5.9
1E9	.81E4	.27E4	-.27E-5	48	8.6	5.6
1E10	.11E5	.27E4	-.27E-6	58	8.6	5.6
1E11	.15E5	.27E4	-.27E-7	67	8.6	5.6

happened to be aligned, resulting in local stress risers. Using a stiffness of $K_n = 1E9$ N/m provides acceptable nodal penetrations and convergence conditions.

To prepare for the final analysis, the last modifications to the model were made. Small changes in mesh density were made to bring the error rate to less than 5% in any area within 10% of yield. Nonlinear material properties using a bilinear, isotropic hardening model for the penetrator and sabot were incorporated, and the final changes in geometry were made. Material properties used in the analysis are found in Table 2. A nodal plot of the final model is displayed in Figure 6 with boundary

Table 2. Material Properties

Material	Density (kg/m ³)	Poisson's Ratio	Young's Modulus (MPa)	Yield Stress (MPa)	Tangent Modulus (MPa)
Tungsten [2]	17,600	0.28	310	1,000	3.1
Aluminum [3]	2,750	0.31	69	490	0.69
Steel	7,850	0.29	207	—	—
Nylon	1,600	0.45	3.4	—	—

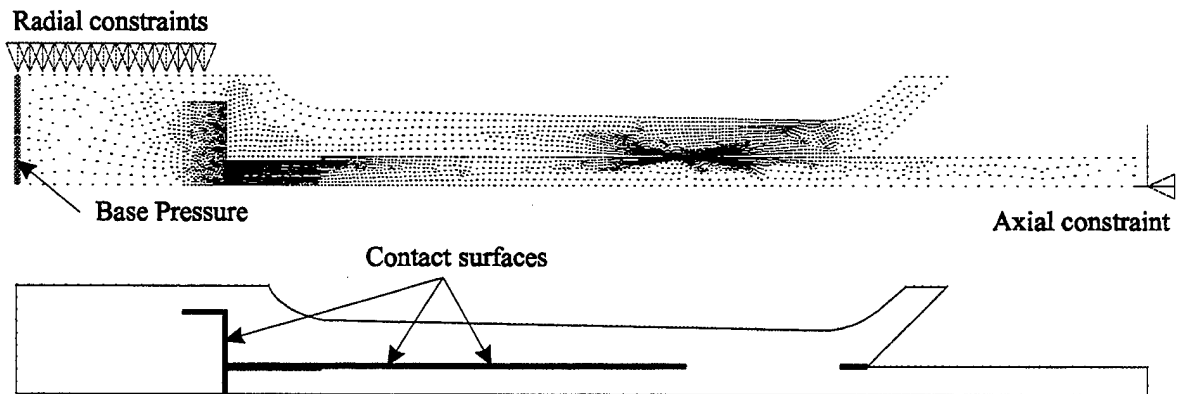


Figure 6. Nodal Plot With Boundary Conditions; Contact Surfaces Have Been Highlighted.

conditions; an edge plot is also provided to show where the contact surfaces exist. Boundary conditions were determined using a projectile mass of 990 g, a charge mass of 700 g, and a breech pressure of 345 MPa, which resulted in a base pressure of 255 MPa and an acceleration of 51,225 g's. Figure 7 shows the resulting effective stress and plastic strain plots.

The results in Figure 7 show a stress concentration in the sabot at the aft end of the grooved region, which was of concern. Even though the plastic strain field surrounding this concentration is relatively small, the high plastic strain and the fact that the groove length (0.21 cm, approximately one-third of the penetrator radius) is comparable to the strain field size indicates possible groove failure. Since the continuous bimetallic interface in the model is actually sixteen 12-pitch annular grooves in the projectile, failure of one groove could lead to failure of other or all grooves.

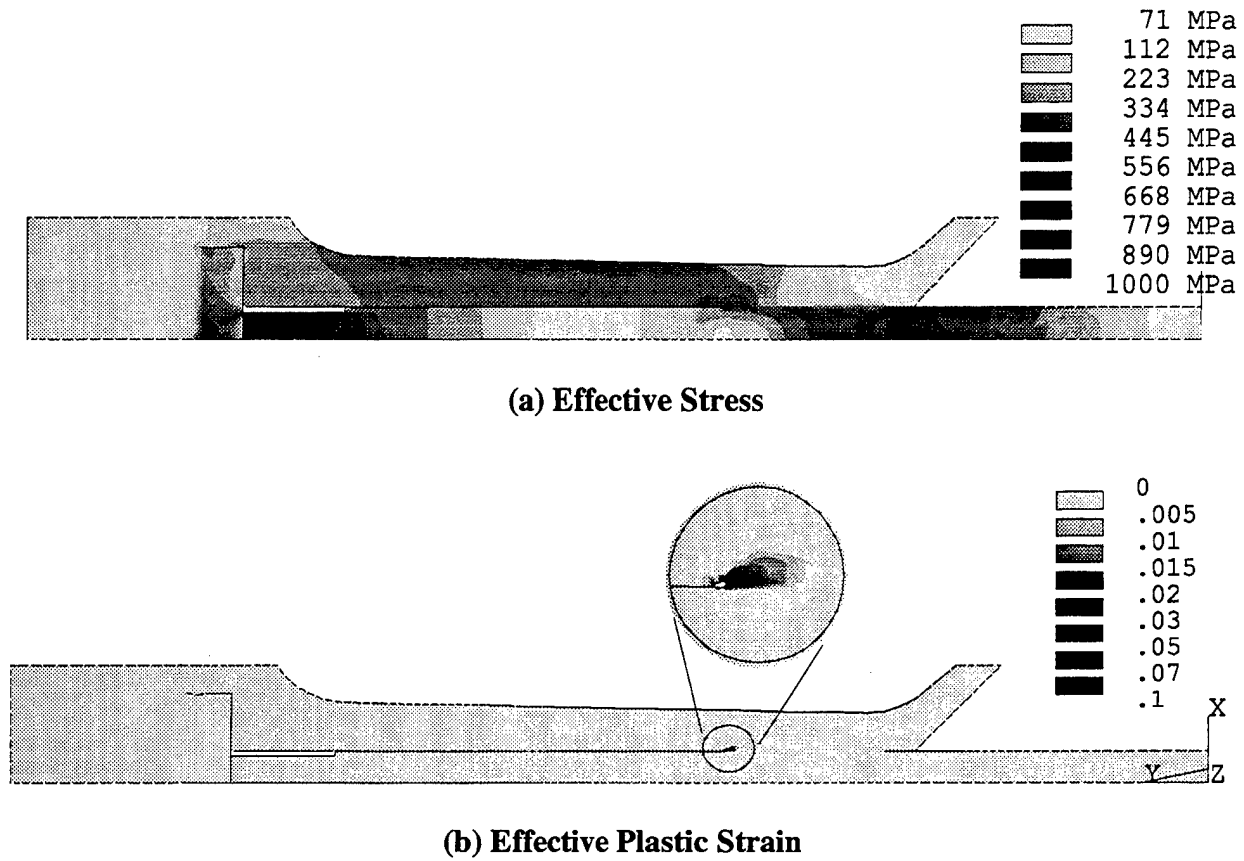


Figure 7. Effective Stress and Plastic Strain Results of the Final Projectile Design.

The loading scheme in this configuration is similar to that of a nut and bolt in tension. The load is distributed across the interface with the maximum load located at the last (aft) groove. As this groove deforms plastically, the load is transferred to the next groove. This process continues until the maximum load is reached, or one or more of the grooves fail.

Using the nut and bolt analogy, the strength of the grooved interface can be compared to the expected load. The assumption made in determining the strength of the interface is that the weaker material, the sabot, will fail in shear. The force required to do this is simply the product of the shear bearing area and the shear yield stress. Using the length (l) and radius (r) of the sabot groove root and the number of grooves (n), the total area ($A_{shear} = 2\pi rln$) under shear can be obtained. Using one-half of the uniaxial yield stress as the yield criteria in shear, the force required for the grooves to fail in shear was computed as 317 kN. The inertial force of the penetrator ($F = ma$) is supported

by the grooves and the pusher plate. Subtracting the sum of the normal contact forces between the penetrator and the pusher plate from the inertial force yields the total force carried by shear in the grooved interface, which is 179 kN, or 56% of the force required to cause a shear failure of the joint. Considering the number of assumptions made, this safety factor of 1.8 may be much less in reality; however, at least the interface appears secure, except for the stress concentration.

The question at this point is whether the magnitude of the stress concentration is real or an artifact of the analysis. Adding grooves into the model may answer the question, but it would merely be an academic exercise since the geometry in this area cannot be changed. The groove profile is determined by the penetrator, and the number of grooves cannot be increased without significant impact on manufacturing methods and cost; therefore, the model and geometry were accepted as is, with only one exception. The gap between the pusher plate and the penetrator dictates the strain throughout the projectile and is difficult to control with exactness because of tolerance stackup; thus, a series of analyses were performed where the gap was varied to determine how sensitive the results were to this parameter. This study also revealed the gap that minimized plastic strain in the projectile and indicated the acceptable manufacturing allowances to use.

Table 3 and Figure 8 display the results of varying the gap size. Figure 8a plots maximum effective plastic strain in both the penetrator tail and the sabot groove sections against the size of the gap. (To illustrate the effects of the stress concentration at the aft end of the sabot grooves, maximum effective plastic strain is plotted for all sabot nodes and for a case where the nodes associated with the stress concentration have been removed.) The data show that as the gap increases, plastic strain in the penetrator decreases but remains relatively constant in the sabot until the penetrator becomes elastic and increases linearly. This trend is repeated in Figure 8b, where the penetrator's inertial force is plotted in its normal (tail) and shear (grooves) components.* The initial expectation of decreasing the load experienced by the penetrator tail by increasing the gap size only

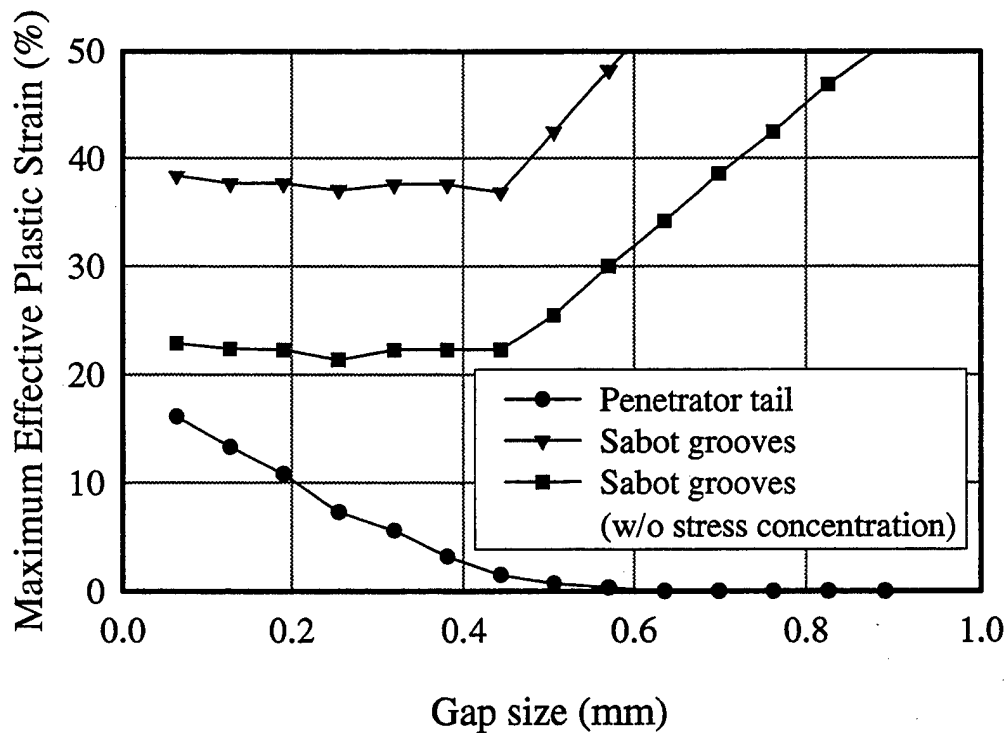
* The initial, slight oscillatory nature of the forces with respect to gap size (as seen in Table 3) is caused by the redistribution of plastic strain from the penetrator centerline to the penetrator radius as the gap increases; while the maximum plastic strain may be decreasing, total plastic strain at the interface is changing.

Table 3. Results From the Gap Size Study

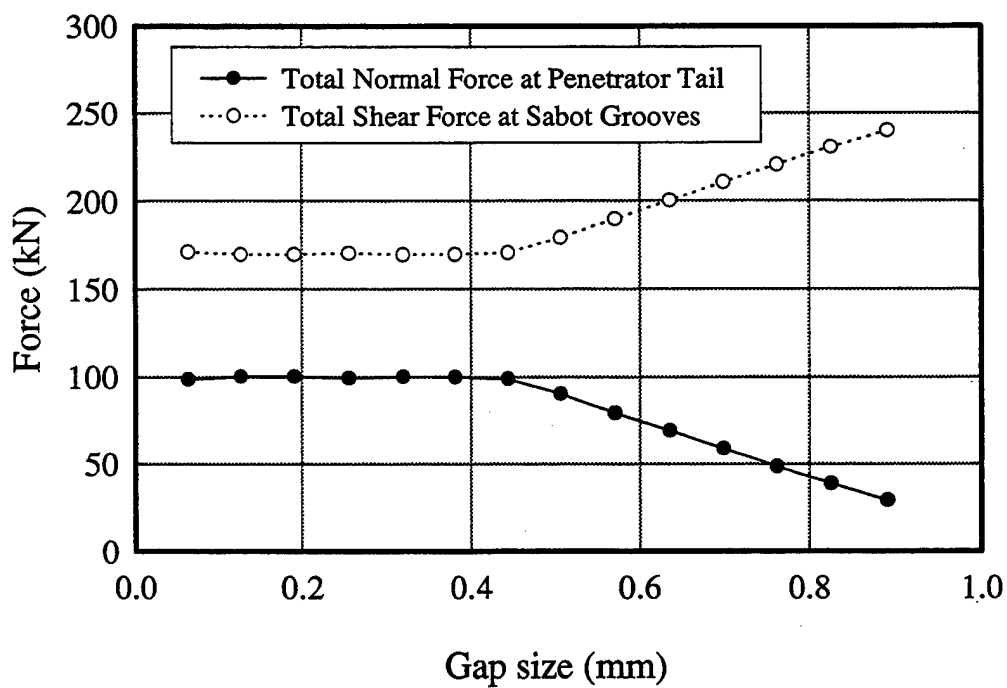
Gap (mm)	Normal Force at Tail (kN)	Shear Force at Grooves (kN)	Maximum Plastic Strain (Penetrator)	Maximum Plastic Strain (Sabot w/Riser)	Maximum Plastic Strain (Sabot w/o Riser)
0.0635	98.1	171.3	0.161	0.384	0.229
0.1270	100.2	169.8	0.133	0.377	0.224
0.1905	100.2	169.7	0.108	0.377	0.223
0.2540	99.5	170.4	0.073	0.371	0.214
0.3175	100.2	169.6	0.056	0.376	0.222
0.3810	99.9	169.8	0.032	0.376	0.223
0.4445	98.9	170.8	0.015	0.369	0.223
0.5080	90.2	179.4	0.007	0.426	0.255
0.5715	79.8	189.8	0.003	0.482	0.300
0.6350	69.2	200.2	0.0	0.544	0.342
0.6985	58.9	210.6	0.0	0.605	0.386
0.7620	48.7	220.7	0.0	0.676	0.425
0.8255	38.8	230.5	0.0	0.742	0.469
0.8890	29.3	239.9	0.0	0.800	0.507

occurs once the penetrator becomes elastic. When the penetrator tail is in the plastic regime, the low-tangent modulus prevents additional load-bearing capability while permitting large displacements (strains) to occur. Thus, until the gap is large enough to remove all plastic deformation, the load distribution between the grooves and the tail remains constant.

Although the size of the plastic strain field in the sabot grooves remained constant as additional load was transferred into the sabot, the stress concentration could not be assumed to be an artifact of the model; on the other hand, the magnitude of the plastic strain most likely did not reflect the actual plastic strain either. Regardless, the bilinear nature of the shear force transmitted to the sabot grooves provided an obvious decision path to select the proper gap size. Since the shear force



(a) Plastic Strains



(b) Penetrator Forces

Figure 8. Plastic Strains and Penetrator Forces as a Function of Gap Size.

transmitted to the sabot grooves was constant and at a minimum while the penetrator tail was plastic, the maximum gap should be near 0.45 mm, which also minimizes the plastic strain in the penetrator tail. Therefore, to leave sufficient allowance for manufacturing and assembly, gap size was specified as 0.254–0.508 mm (0.010–0.020 in). The results in Figure 6 correspond to a gap of 0.508 mm.

3. Experimental Verification

A three-shot verification program was conducted as a proof-of-principle test of the projectile design prior to manufacturing the remaining sabots. Figure 9 shows the third projectile tested, which differed slightly from the first two in that a maraging steel sleeve was added to the penetrator tail for additional support. Figure 10 depicts the launch state of a projectile by showing a flash radiograph taken just after muzzle exit; it is representative of all three tests. For the first two tests, the desired velocity was achieved and the accelerations approached the projectile's acceleration, as depicted in Figure 1b (see Table 4). Since the penetrators were straight and the sabot discard symmetric, it appeared that the projectile was a success. However, detailed examination of the radiographs taken just prior to impact did not show the section of decreased diameter at the tail of the penetrator, as shown in Figures 1a and 2 (see also Figures 11 and 12). In both tests, a hint of the shoulder is still evident and a slight bulge is even apparent in Figure 12. Additional measurements from the radiographs showed that the tail of each penetrator had permanently deformed, decreasing penetrator length by approximately 7.5 mm.

Without attempting to explain the previous two projectile failures, a maraging steel sleeve was added to the back of the penetrator to prevent permanent deformation for the last test. Figure 13 displays the impact radiograph of this test, indicating no visible or measurable deformation. However, since the measured breech pressure for this test was 35% lower than the previous tests, it cannot be stated conclusively that this modification improved the projectile, even though the projectile and propellant masses were the same. Since the velocity was 8% lower than expected, the pressure measurement was most likely accurate. Regardless, the projectile was deemed only partially successful and the customer decided to pursue other options.

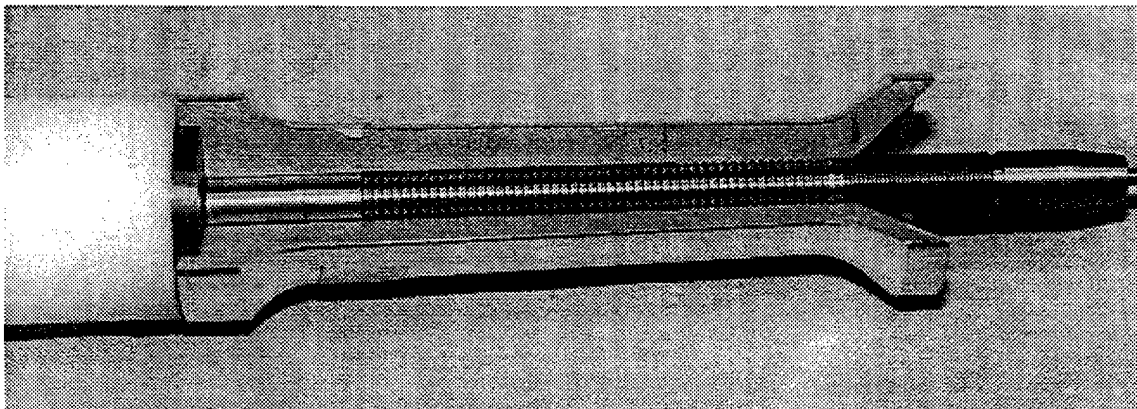


Figure 9. Photograph of the Third Projectile Tested (Experiment No. 920).

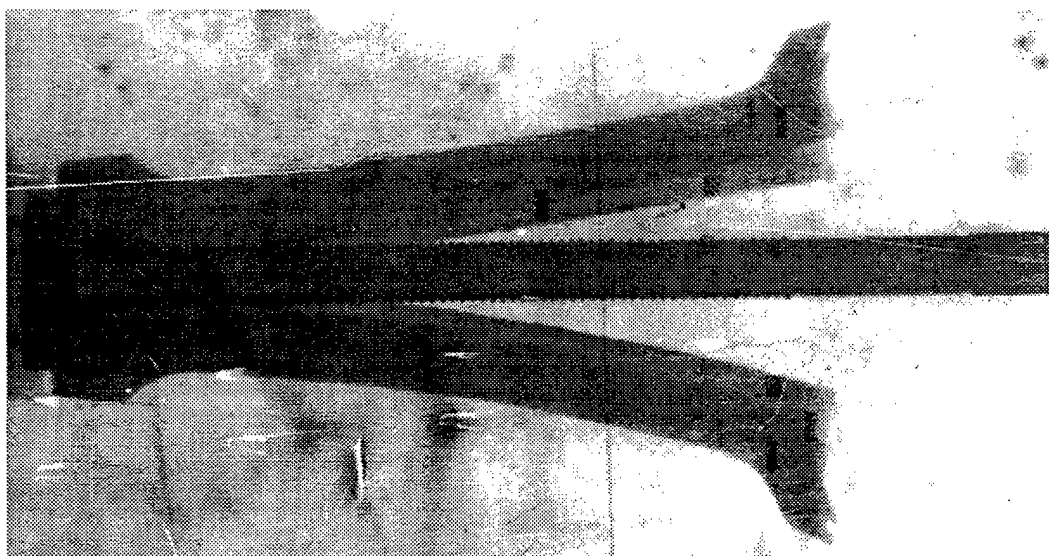


Figure 10. Flash Radiograph of Experiment No. 920 at Muzzle Exit.

Table 4. Experimental Results

Experiment No.	M_{proj} (kg)	M_{rod} (kg)	M_{prop} (kg)	P_{brech} (MPa)	P_{base} (MPa)	Acceleration (g's)	σ (MPa)	Velocity (m/s)
539	0.482	0.292	0.325	193	144	38270	1154	1184
815	0.925	0.445	0.680	383	280	60587	2733	1374
918	0.969	0.482	0.700	334	245	50683	2286	1360
919	0.971	0.482	0.695	365	269	55408	2499	1368
920	0.970	0.495	0.695	221	163	33573	1514	1247

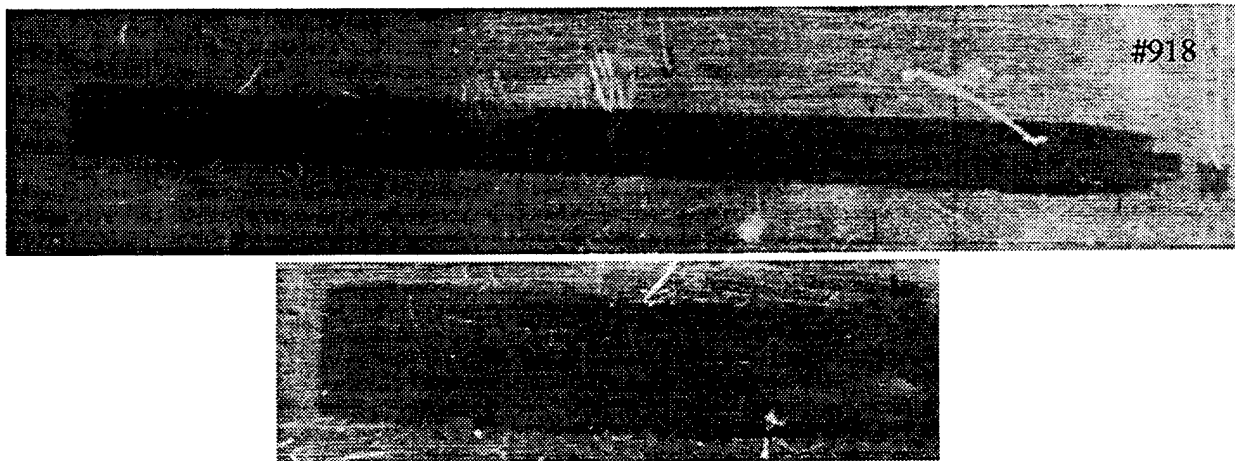


Figure 11. Flash Radiograph of Experiment No. 918 Just Before Target Impact.

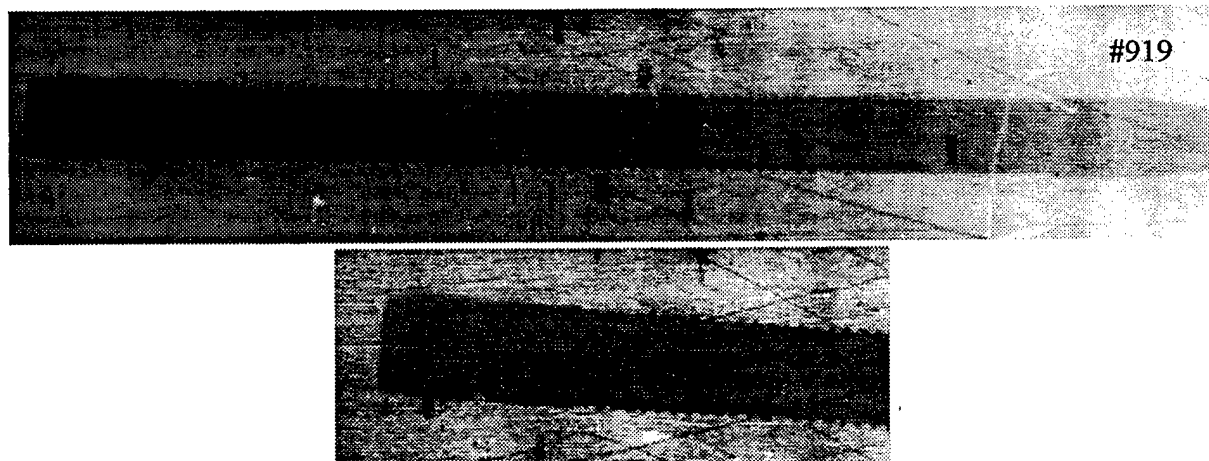


Figure 12. Flash Radiograph of Experiment No. 919 Just Before Target Impact.

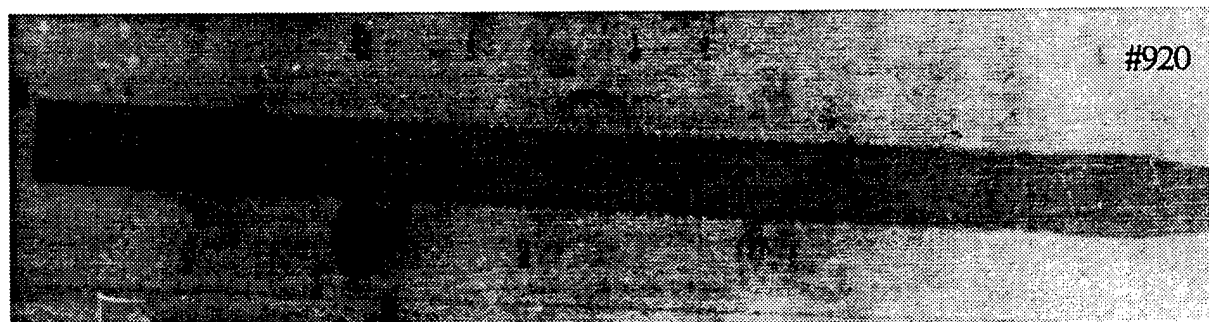


Figure 13. Flash Radiograph of Experiment No. 920 Just Before Target Impact.

4. Post-Test Analyses

Several analyses were performed to determine why the projectile failed. The working assumption is that the sabot grooves failed prior to maximum acceleration, converting the projectile to a push launch system. The increased rigidity of the aluminum sabot provided sufficient radial support to keep the penetrator in a column, eliminating potential nonaxial loads and preventing column buckling. The sabot also provided radial constraint to the back of the penetrator, acted as a die while the penetrator was pressed into the pusher plate, and controlled and limited the amount of deformation.

To verify that the sabot grooves failed, groove geometry was added into the model so that the stress state could be examined in each groove. Instead of using a cut-boundary submodel, this geometry was added to the entire model to avoid dealing with potential problems arising from transferring the boundary conditions on a long, path-sensitive load curve. Furthermore, it was easier and less time consuming to create a dense mesh and let the problem run.

To prevent node penetrations along the flank and at the corners, the groove geometry had 0° pressure and 45° clearance flanks with contact surfaces on and around the 0° pressure flank. To minimize the number of elements, contact surfaces were not applied to the clearance flank. Lastly, since the penetrator was now connected to the rest of the model by contact elements only, extra care was taken when loading the model to ensure sufficient stiffness and to avoid an ill-conditioned stiffness matrix. Base pressure and acceleration were determined using the results from experiment 918 (see Table 4). The geometry used in this analysis is displayed in Figure 14, along with plots of shear stress and effective plastic strain of the last five sabot grooves. With effective plastic strain above 10% in the last groove and shear stresses above the Tresca yield criteria (240 MPa) at the corners of the groove root, the last (aft) groove probably failed. But, the bilinear nature of the material model permits additional loading to occur instead of transferring the entire load to the other grooves.

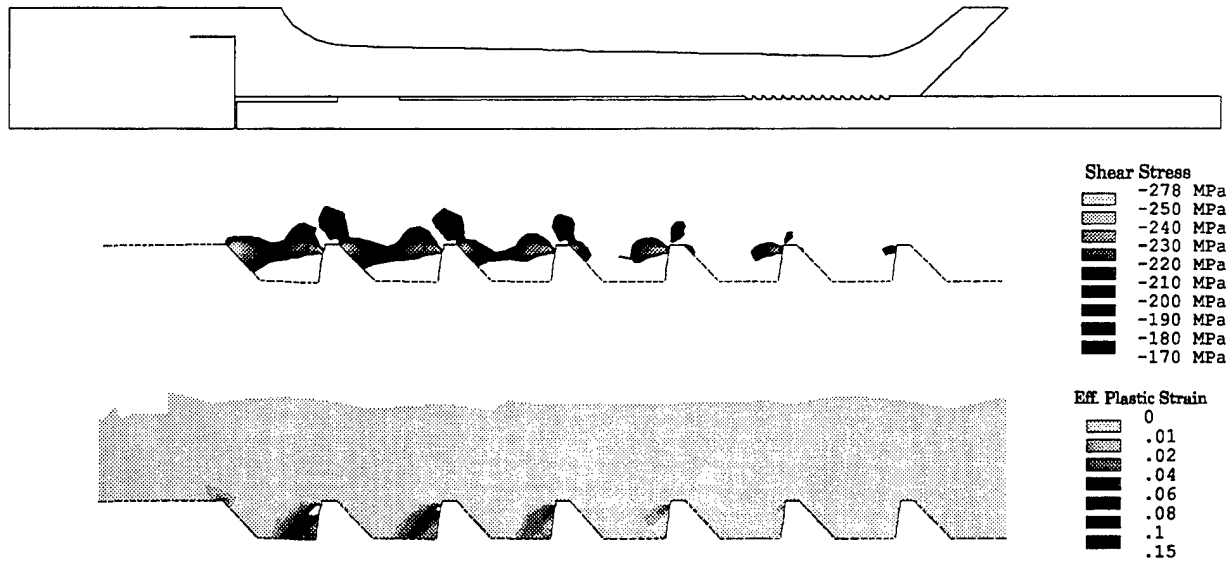
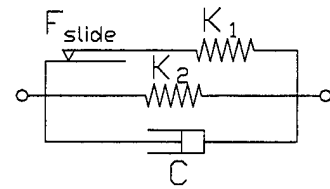
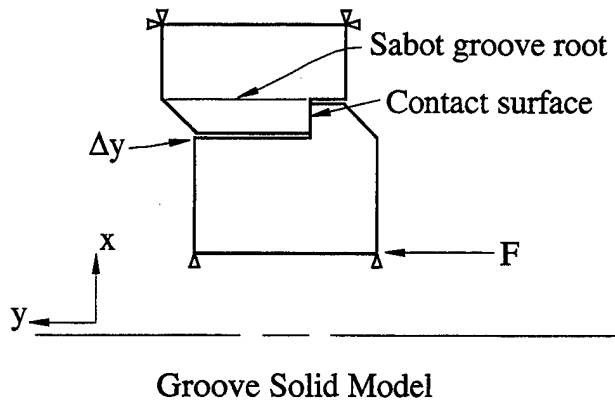


Figure 14. Shear Stress and Effective Plastic Strain Results Using Exact Groove Geometry.

Decreasing the tangent modulus or using a different material to model groove failure proved unsuccessful and consumed significant computer time; therefore, the grooves were replaced by spring elements (COMBIN40) that contain a breakaway feature. Regularly spaced coincident nodes were placed on the penetrator/sabot interface and 16 spring elements oriented in the axial direction were added. Also, the nodes were coupled in the radial direction to prevent rotation. To determine a spring constant (K_1) for the COMBIN40 elements, a model of one penetrator and one sabot groove was constructed (see Figure 15). The sabot groove was fixed in space, and the penetrator groove was given an axial load (F). Once a minimum contact element stiffness was determined (based on node penetration), an axial displacement on the penetrator groove (Δy) in a low-stress region was obtained. The spring constant is simply $k_1 = F/\Delta y$. To obtain the force at which sliding occurs (F_{slide}), the area of the sabot groove root ($A = 2\pi rl$) was multiplied by the shear strength (τ) of the aluminum. Using these assumptions for the spring elements, the grooves did not fail. However, when F_{slide} was decreased by 45% to cause the last (aft) groove to fail, the sudden increase in load on the preceding grooves caused each of them in turn to fail, unzipping the interface. Considering the stress concentrations at the corners of the groove root, a factor of two difference between the assumptions and the finite element model is not unreasonable. Finally, the simple modification of



COMBIN40 Element

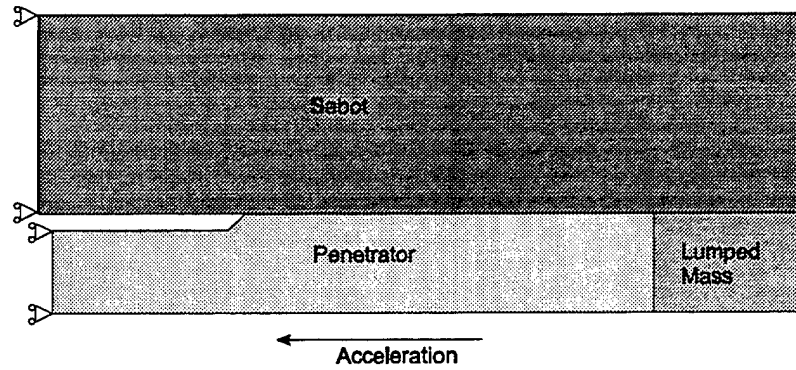
$$K_1 = \frac{F}{\Delta y} \quad F_{\text{slide}} = 2\pi r l \tau$$

Figure 15. Solid Model Used in a Groove Stiffness Analysis to Determine K_1 and F_{slide} .

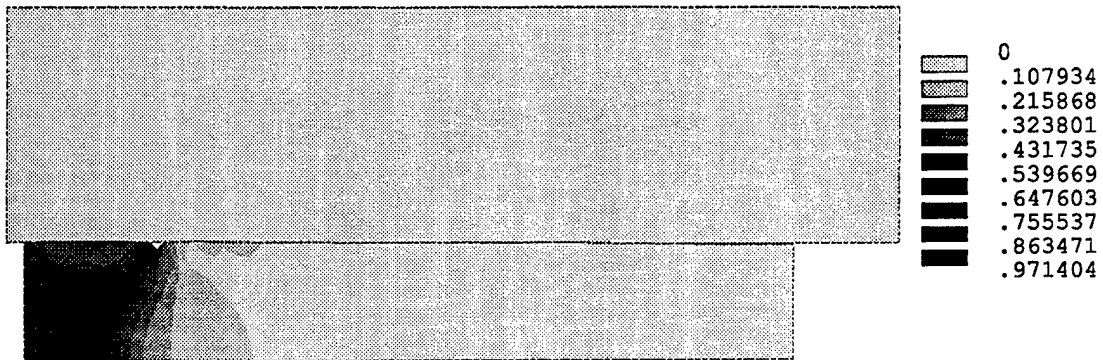
removing one (or more) penetrator groove(s) behind the last sabot groove would have permitted an increase in thickness of at least 250% for the last sabot groove, providing adequate strength to resist failure.

With a plausible explanation of the failure in hand, a final analysis was performed to confirm that the amount of plastic deformation observed in the radiographs was reasonable. The aft portion of the penetrator was modeled with the aft end constrained in the axial direction. (Elements at the front of the penetrator used a modified density to obtain the proper mass properties.) A thick aluminum tube was placed around the penetrator to represent the sabot, and gap elements were placed between the parts. Since plastic strains beyond 30% were expected, quadrilateral, viscoplastic elements (VICSO106) were used in the penetrator with the same bilinear isotropic material model previously used. Finally, the step increase in diameter was changed to a 45° taper, which permitted the penetrator to be defined by three quadrilateral areas for mapped meshing and removed the need for a locally dense mesh. Contact elements were placed between the 45° taper and the penetrator tail to ensure that penetrator elements did not overlap each other as the deformation occurred.

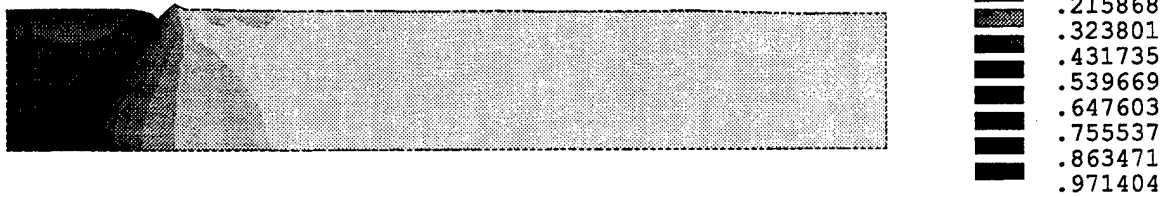
The solid model and the results of this analysis are displayed in Figure 16. The displacement plot in Figure 16 shows that the penetrator tail has nearly upset completely to the diameter of the aluminum die. The remaining plots show effective plastic strain of the penetrator and die. These results were plotted with a displacement scale factor of one; the penetrator shape agrees well with



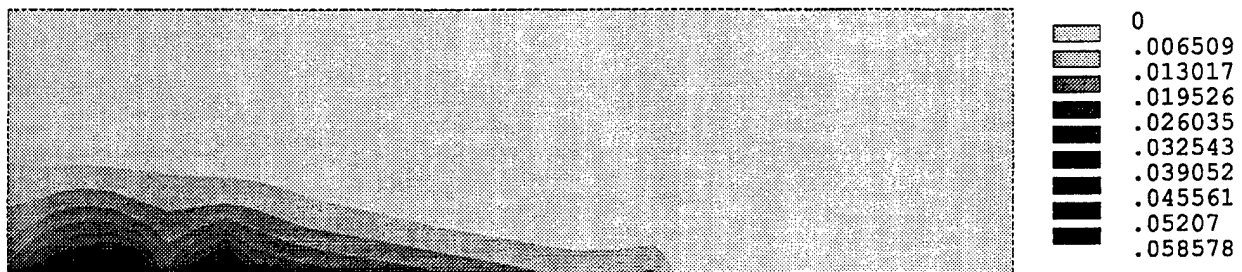
Solid Model



Effective Plastic Strain and Displacement Plot



Effective Plastic Strain (Penetrator Only)



Effective Plastic Strain (Aluminum Die Only)

Figure 16. Displacement and Effective Plastic Strain Plots of the Penetrator Tail Deformation Analysis.

the radiographs (Figures 11 and 12). In the radiographs, a hint of the shoulder is present in the form of a notch present on each radiograph. The bulges observed in the radiographs are also consistent with the plastic deformation of the supporting aluminum structure (Figure 16). After unloading the model, the penetrator decreased in length by 6.5 mm, as compared to the 7.5 mm change measured on the radiographs. Assuming a conservation of volume and that permanent deformation was restricted to the area of reduced diameter, a computed deformation of 6.8 mm was established. These results yield excellent agreement between the experimental data and modeling results, and they provide closure on the failure analysis.

5. Conclusions

The engineering analysis code ANSYS was used to design a sabot to launch a penetrator from a 50-mm cannon that had failed catastrophically in a push launch sabot. Conceptually, this sabot was different from traditional push and traction launch sabot systems in that a combination of both technologies was used. During experimental trials, a sabot failure permitted significant plastic deformation of the penetrator, but kept it from breaking. Sabot failure was later characterized and modeled with ANSYS, which validated the sabot failure mode and predicted the amount of permanent penetrator deformation. Finally, these analyses and experiments proved the feasibility of push launching high aspect ratio penetrators at high velocity, using the sabot to control plastic penetrator deformation. In fact, drag flares can even be swaged into place at launch.

INTENTIONALLY LEFT BLANK.

6. References

1. ANSYS, Inc. *ANSYS Rev 5.4 User's Manuals*. Canonsburg, PA: ANSYS, 1997.
2. Dudder, G. Unpublished data. Battelle Pacific Northwest Laboratory, Richland, WA, 1989.
3. Belfour Stulen, Inc. *Department of Defense Aerospace Structural Metals Handbook*. Columbus, OH: Belfour Stulen, 1980.

INTENTIONALLY LEFT BLANK.

NO. OF
COPIES ORGANIZATION

2 DEFENSE TECHNICAL
INFORMATION CENTER
DTIC DDA
8725 JOHN J KINGMAN RD
STE 0944
FT BELVOIR VA 22060-6218

1 HQDA
DAMO FDT
400 ARMY PENTAGON
WASHINGTON DC 20310-0460

1 OSD
OUSD(A&T)/ODDDR&E(R)
R J TREW
THE PENTAGON
WASHINGTON DC 20301-7100

1 DPTY CG FOR RDA
US ARMY MATERIEL CMD
AMCRDA
5001 EISENHOWER AVE
ALEXANDRIA VA 22333-0001

1 INST FOR ADVNCD TCHNLGY
THE UNIV OF TEXAS AT AUSTIN
PO BOX 202797
AUSTIN TX 78720-2797

1 DARPA
B KASPAR
3701 N FAIRFAX DR
ARLINGTON VA 22203-1714

1 NAVAL SURFACE WARFARE CTR
CODE B07 J PENNELLA
17320 DAHLGREN RD
BLDG 1470 RM 1101
DAHLGREN VA 22448-5100

1 US MILITARY ACADEMY
MATH SCI CTR OF EXCELLENCE
MADN MATH
MAJ HUBER
THAYER HALL
WEST POINT NY 10996-1786

NO. OF
COPIES ORGANIZATION

1 DIRECTOR
US ARMY RESEARCH LAB
AMSRL D
D R SMITH
2800 POWDER MILL RD
ADELPHI MD 20783-1197

1 DIRECTOR
US ARMY RESEARCH LAB
AMSRL DD
2800 POWDER MILL RD
ADELPHI MD 20783-1197

1 DIRECTOR
US ARMY RESEARCH LAB
AMSRL CI AI R (RECORDS MGMT)
2800 POWDER MILL RD
ADELPHI MD 20783-1145

3 DIRECTOR
US ARMY RESEARCH LAB
AMSRL CI LL
2800 POWDER MILL RD
ADELPHI MD 20783-1145

1 DIRECTOR
US ARMY RESEARCH LAB
AMSRL CI AP
2800 POWDER MILL RD
ADELPHI MD 20783-1197

ABERDEEN PROVING GROUND

4 DIR USARL
AMSRL CI LP (BLDG 305)

<u>NO. OF COPIES</u>	<u>ORGANIZATION</u>
2	COMMANDER US ARMY ARDEC AMSTA CCH S MUSALLI R CARR PICATINNY ARSENAL NJ 07806-5000
1	COMMANDER US ARMY ARDEC AMSTA AR E FENNEL PICATINNY ARSENAL NJ 07806-5000
2	COMMANDER DARPA J KELLY B WILCOX 3701 F FAIRFAX DR ARLINGTON VA 22203-1714
2	COMMANDER WL FIV A MAYER WL SLMLBM S DONALDSON 2941 P STREET STE 1 WRIGHT PATTERSON AFB OH 45433
4	DIRECTOR LLNL R CHRISTENSEN S DETERESA F MAGNESS M FINGER PO BOX 808 LIVERMORE CA 94550
1	LANL J REPPA MS F668 PO BOX 1633 LOS ALAMOS NM 87545
1	LLNL M MURPHY PO BOX 808 L 282 LIVERMORE CA 94550

<u>NO. OF COPIES</u>	<u>ORGANIZATION</u>
4	DIRECTOR SANDIA NATIONAL LAB APPLIED MECHANICS DEPT DIVISION 8241 W KAWAHARA K PERANO D DAWSON P NIELAN PO BOX 969 LIVERMORE CA 94550-0096
1	BATTELLE C R HARGREAVES 505 KING AVE COLUMBUS OH 43201-2681
2	PACIFIC NORTHWEST LAB M SMITH R SHIPPELL PO BOX 999 RICHLAND WA 99352
1	AAI CORPORATION T G STASTNY PO BOX 126 HUNT VALLEY MD 21030-0126
2	ALLIANT TECHSYSTEMS INC C CANDLAND D KAMDAR 600 SECOND ST NE HOPKINS MN 55343-8384
3	INSTITUTE FOR ADVANCED TECH S BLESS P SULLIVAN W REINECKE 4030 2 W BRAKER LN AUSTIN TX 78759
2	SOUTHWEST RSCH INSTITUTE C ANDERSON J RIEGEL 6220 CULEBRA RD PO DRAWER 28510 SAN ANTONIO TX 78228-0510

<u>NO. OF COPIES</u>	<u>ORGANIZATION</u>
1	DYNA EAST CORPORATION DR P C CHOU 3201 ARCH ST PHILADELPHIA PA 19104-2711
1	OLIN CORPORATION FLINCHBAGH DIV E STEINER PO BOX 127 RED LION PA 17356
1	OLIN CORPORATION L WHITMORE 10101 9TH ST NORTH ST PETERSBURG FL 33702

<u>NO. OF COPIES</u>	<u>ORGANIZATION</u>
	<u>ABERDEEN PROVING GROUND</u>
36	DIR USARL AMSRL WM B A HORST E SCHMIDT AMSRL WM BC P PLOSTINS J NEWILL S WILKERSON AMSRL WM MB W DRYSDALE L BURTON C HOPPEL R KASTE AMSRL WM MD W DE ROSSET AMSRL WM T B BURNS AMSRL WM TA W GILLICH W BRUCHEY T HAVEL M KEELE AMSRL WM TC R COATES E KENNEDY L MAGNESS R MUDD G SILSBY B SORENSEN (10 CPS) AMSRL WM TD D DIETRICH T FARRAND K FRANK AMSRL WM BA F BRANDON W D AMICO AMSRL WM BR J BORNSTEIN

INTENTIONALLY LEFT BLANK.

REPORT DOCUMENTATION PAGE			Form Approved OMB No. 0704-0188	
Public reporting burden for this collection of information is estimated to average 1 hour per response, including the time for reviewing instructions, searching existing data sources, gathering and maintaining the data needed, and completing and reviewing the collection of information. Send comments regarding this burden estimate or any other aspect of this collection of information, including suggestions for reducing this burden, to Washington Headquarters Services, Directorate for Information Operations and Reports, 1215 Jefferson Davis Highway, Suite 1204, Arlington, VA 22202-4302, and to the Office of Management and Budget, Paperwork Reduction Project (0704-0188), Washington, DC 20503.				
1. AGENCY USE ONLY (Leave blank)		2. REPORT DATE August 2000		3. REPORT TYPE AND DATES COVERED Final, Apr 95 - Mar 96
4. TITLE AND SUBTITLE Design, Analysis, and Verification of a 50-mm Push/Traction Sabot			5. FUNDING NUMBERS 1L162618AH80	
6. AUTHOR(S) Brett Sorensen				
7. PERFORMING ORGANIZATION NAME(S) AND ADDRESS(ES) U.S. Army Research Laboratory ATTN: AMSRL-WM-TC Aberdeen Proving Ground, MD 21005-5066			8. PERFORMING ORGANIZATION REPORT NUMBER ARL-TR-2292	
9. SPONSORING/MONITORING AGENCY NAME(S) AND ADDRESS(ES)			10. SPONSORING/MONITORING AGENCY REPORT NUMBER	
11. SUPPLEMENTARY NOTES				
12a. DISTRIBUTION/AVAILABILITY STATEMENT Approved for public release; distribution is unlimited.			12b. DISTRIBUTION CODE	
13. ABSTRACT (Maximum 200 words) This report presents the design and analysis of a kinetic energy projectile for a 50-mm cannon using finite element techniques. A combination of push and traction launch concepts was used to configure a sabot for a penetrator that experienced catastrophic failure using a push launch sabot system. A parametric model with both plasticity and nonlinear elements was used to model the projectile that experienced accelerations exceeding 50,000 g's. Experimental tests showed marginal success in that a sabot failure permitted significant plastic deformation of the penetrator. Additional post-test analyses predicted the failure mode and the amount of plastic penetrator deformation demonstrated in the experiments.				
14. SUBJECT TERMS sabot, sabot design, kinetic energy projectiles, finite element analysis			15. NUMBER OF PAGES 29	
			16. PRICE CODE	
17. SECURITY CLASSIFICATION OF REPORT UNCLASSIFIED	18. SECURITY CLASSIFICATION OF THIS PAGE UNCLASSIFIED	19. SECURITY CLASSIFICATION OF ABSTRACT UNCLASSIFIED	20. LIMITATION OF ABSTRACT UL	

INTENTIONALLY LEFT BLANK.